Gate-Tunable Antiferromagnetic Chern Insulator in Twisted Bilayer Transition Metal Dichalcogenides

Xiaoyu Liu,[1,*] Yuchi He,[2,*] Chong Wang,[1] Xiao-Wei Zhang,[1] Ting Cao,[1,†] and Di Xiao[1,3,‡]
[1]Department of Materials Science and Engineering, University of Washington, Seattle, Washington 98195, USA
[2]Rudolf Peierls Centre for Theoretical Physics, Clarendon Laboratory, Parks Road, Oxford OX1 3PU, United Kingdom
[3]Department of Physics, University of Washington, Seattle, Washington 98195, USA

(Received 14 August 2023; revised 19 January 2024; accepted 10 March 2024; published 3 April 2024)

A series of recent experimental works on twisted $MoTe_2$ homobilayers have unveiled an abundance of exotic states in this system. Valley-polarized quantum anomalous Hall states have been identified at hole doping of $\nu = -1$, and the fractional quantum anomalous Hall effect is observed at $\nu = -2/3$ and $\nu = -3/5$. In this Letter, we investigate the electronic properties of AA-stacked twisted bilayer $MoTe_2$ at $\nu = -2$ by k-space Hartree-Fock calculations. We identify a series of phases, among which a noteworthy phase is the antiferromagnetic Chern insulator, stabilized by an external electric field. We attribute the existence of this Chern insulator to an antiferromagnetic instability at a topological phase transition between the quantum spin hall phase and a band insulator phase. Our research proposes the potential of realizing a Chern insulator beyond $\nu = -1$, and contributes fresh perspectives on the interplay between band topology and electron-electron correlations in moiré superlattices.

DOI: 10.1103/PhysRevLett.132.146401

Introduction.—Since the experimental discovery of correlated states and superconductivity in twisted bilayer graphene [1,2], two-dimensional moiré superlattices have emerged as a revolutionary platform in the study of electron-electron correlations. Apart from graphene moiré superlattices, transition metal dichalcogenides (TMD) moiré superlattices have been under intensive investigation due to the reduced number of degrees of freedom [3,4]. For example, heterobilayer TMD moiré superlattices have been found to host magnetic phases [5–8], charge ordered phases [5,9–11] and quantum anomalous Hall states [12–18]. Recently, there has been a surge in research focused on homobilayer TMD moiré superlattices [19–24]. Compared with heterobilayers, homobilayer TMD moiré superlattices host intrinsic topological band structures [4,25]. Moreover, both layers' electrons actively contribute to the low-energy physics for homobilayers, which provides a unique opportunity to tune the electronic properties with an out-of-plane electric field [22,26].

Recently, a series of works on twisted $MoTe_2$ homobilayers ($tMoTe_2$) have unveiled an abundance of topological states in this system. At hole doping $\nu = -1$ (one hole per moiré unit cell), valley-polarized quantum anomalous Hall states are observed [23,27–29]. At $\nu = -2/3$ and $\nu = -3/5$, a fractional Chern insulator is observed at zero magnetic field [23,27–29]. The emergence of these states arises from quenched kinetic energy in the flat bands [30–32]. Following the same logic, it would appear that there might not be as many interesting observations at $\nu = -2$, for which the flat bands are completely filled. In this scenario, for electron-electron interactions to play a significant role in low-energy dynamics, the interaction energy has to overcome the band gap. Fortunately, the band gap can be substantially reduced by an external electric field, hinting at the potential for gate-tunable correlated states in twisted $tMoTe_2$. Such prospects add a captivating dimension to the exploration of this fascinating material.

In this Letter, we investigate the electronic properties of AA-stacked $tMoTe_2$ at $\nu = -2$ by k-space Hartree-Fock calculations. The phase diagram of this system reveals four distinct states: an antiferromagnetic Chern insulator, an in-plane antiferromagnetic phase, a quantum spin hall (QSH) phase, and a trivial band insulator (BI). The existence of the in-plane antiferromagnetic phase can be explained by a spin model. The emergence of the antiferromagnetic Chern insulator is attributed to an instability of the phase boundary between the QSH and the BI phases with respect to an antiferromagnetic perturbation under a sufficiently large Coulomb interaction. The antiferromagnetic Chern insulator exists across different twist angles, with the topmost two moiré bands exhibiting distinct Chern numbers at different angles. In addition, we verify the existence of the antiferromagnetic Chern insulator phase by density matrix renormalization group (DMRG) calculations [33,34]. Our Letter points out the possibility of realizing a Chern insulator beyond $\nu = -1$ and provides new insights into the interplay between the band topology and electron-electron correlations in moiré superlattices.

Method.—In monolayer $MoTe_2$, the conduction and valence band edges are located at the corners of the Brillouin zone, i.e., the K and K' points. Owing to strong spin-orbit interaction, electrons in the K and K' valleys

have opposite spins [35]. The major effect of the moiré superlattice is to induce coupling between Bloch functions separated by moiré reciprocal lattice vectors, which is captured by a continuum model. The separation between the K and K' points is much larger than the length scale of the moiré Brillouin zone (mBZ), such that the continuum model is block diagonal in the valley indices. For the K valley, the continuum model Hamiltonian reads as [4,25]

$$H_K = -\frac{\hbar^2}{2m^*}\begin{pmatrix} (\boldsymbol{k}-\boldsymbol{\kappa}_+)^2 & 0 \\ 0 & (\boldsymbol{k}-\boldsymbol{\kappa}_-)^2 \end{pmatrix} + \begin{pmatrix} \Delta_b(\boldsymbol{r})+\Delta_D/2 & \Delta_T(\boldsymbol{r}) \\ \Delta_T^\dagger(\boldsymbol{r}) & \Delta_t(\boldsymbol{r})-\Delta_D/2 \end{pmatrix}, \quad (1)$$

where the intralayer and interlayer moiré potentials are $\Delta_{b/t}(\boldsymbol{r}) = 2V\sum_{i=1,3,5}\cos(\boldsymbol{G}_i\cdot\boldsymbol{r}\pm\phi)$, and $\Delta_T = w(1+e^{-i\boldsymbol{G}_2\cdot\boldsymbol{r}}+e^{-i\boldsymbol{G}_3\cdot\boldsymbol{r}})$, respectively. $\boldsymbol{G}_i = (4\pi/\sqrt{3}a_M)\{\cos[(i-1)/3]\pi, \sin[(i-1)/3]\pi\}$ are moiré reciprocal lattice vectors with a_M being the moiré lattice constant. $\boldsymbol{\kappa}_+ = 2\boldsymbol{G}_1/3-\boldsymbol{G}_2/3$ and $\boldsymbol{\kappa}_- = \boldsymbol{G}_1/3+\boldsymbol{G}_2/3$ are the mBZ corners. m^* is the effective mass and is taken as $0.6m_e$, where m_e is the free electron mass. Layer-differentiating potential proportional to Δ_D is included in H_K to take into account the out-of-plane electric field. For the K' valley, the continuum model Hamiltonian can be deduced by the acting time reversal operator on H_K. The parameters for the continuum model are fitted from large-scale density functional theory calculations [31]. Specifically, $(V,\phi,w) = (20.8\text{ meV}, 107.7°, -23.8\text{ meV})$.

To investigate the effect of electron-electron interaction, we carry out self-consistent Hartree-Fock calculations based on the continuum model. The solution of the continuum model is the envelope function of the atomistic wave function, and the envelope function is expanded as superposition of plane waves. In the basis of the plane waves (labeled by momentum $\boldsymbol{k}$), the electron-electron interaction reads as

$$H_{\text{int}} = \frac{1}{2A}\sum_{l,l',\tau,\tau',\boldsymbol{k},\boldsymbol{k}',\boldsymbol{q}} V_{ll'}(\boldsymbol{q})c^\dagger_{l\tau\boldsymbol{k}+\boldsymbol{q}}c^\dagger_{l'\tau'\boldsymbol{k}'-\boldsymbol{q}}c_{l'\tau'\boldsymbol{k}'}c_{l\tau\boldsymbol{k}}, \quad (2)$$

where A is the area of the system, l and l' label layers, and τ and τ' label valleys. The Coulomb interaction takes the form [36]

$$V_{ll'}(\boldsymbol{q}) = \frac{e^2}{2\epsilon\epsilon_0|\boldsymbol{q}|}\left[\tanh(d_{\text{gate}}|\boldsymbol{q}|)+(1-\delta_{ll'})(e^{-d|\boldsymbol{q}|}-1)\right], \quad (3)$$

where ϵ is the relative dielectric constant, ϵ_0 is the vacuum permittivity, d_{gate} is the distance between the sample and the symmetric metal gate, and d is the distance between the two monolayers. The interlayer Coulomb interaction is reduced from the intralayer Coulomb interaction by $e^{-d|\boldsymbol{q}|}-1$. This correction is only valid for $d \ll d_{\text{gate}}$ [36]. The self-consistent Hartree-Fock calculations are performed in the reciprocal space without projecting the interaction to bands near the charge neutrality point.

Phase diagram at 3.89°.—At twist angle 3.89°, the noninteracting single-particle band structure is presented in Fig. 1. The topmost moiré band from the K (K') valley has Chern number 1 (−1), and the second moiré band has the opposite Chern number. Figure 1(c) presents the Hartree-Fock phase diagram as a function of ϵ and Δ_D at twist angle $\theta = 3.89°$. For a noninteracting limit ($\epsilon\to\infty$), the system exhibits a QSH phase at $\Delta_D = 0$. The QSH state can be turned into a trivial BI state via band inversions at the $\boldsymbol{\kappa}_+$ and $\boldsymbol{\kappa}_-$ point for large Δ_D (details in the Supplemental Material [37]). As the interacting strength increases, two more phases emerge. With $\Delta_D = 0$, the AFMxy phase is stabilized for small ϵ. In this phase, the two sublattices possess opposite magnetic moments in the x-y plane [inset of Fig. 1(c)]. For larger Δ_D, the orientation of the magnetic moment changes to the $\pm z$ direction, and the AFMz phase is stabilized [inset of Fig. 1(c)]. We have also performed Hartree-Fock calculations in a $\sqrt{3}\times\sqrt{3}$ supercell, and no translational symmetry breaking phases are found. The phase transitions from AFMxy to AFMz and from AFMz to BI are characterized as first-order phase transitions whereas the transition from QSH to BI is a second-order phase transition. Based on our numerical evidence, the transition between QSH and AFMxy is more likely to be a second-order phase transition (Supplemental Material [37]).

Most interestingly, the AFMz phase is an antiferromagnetic Chern insulator. The quasiparticle band structure of AFMz features two massive Dirac points [Fig. 1(d)] at $\boldsymbol{\kappa}_+$ and $\boldsymbol{\kappa}_-$, both of which contribute π Berry flux, and the total Chern number is 1.

A real-space picture can help one understand the phase diagram in Fig. 1(c). The moiré potential has local minimums at the MX (XM) stacking for the top and bottom layers, respectively, where the Mo (Te) atoms sit on top of the Te (Mo) atoms. As shown in Fig. 1(a), these local minimums form a buckled honeycomb lattice, where the A (B) sublattices are from the top (bottom) layer. Therefore, $tMoTe_2$ can be qualitatively understood as a Kane-Mele-Hubbard model [39–42]:

$$\begin{aligned} H_{\text{KMH}} &= H_{\text{single}} + \sum_i U n_{i\uparrow}n_{i\downarrow}, \\ H_{\text{single}} &= \sum_{\langle i,j\rangle,\sigma} t_1 c^\dagger_{i\sigma}c_{j\sigma} + \sum_{\langle\langle i,j\rangle\rangle,\sigma} t_2 e^{i\sigma\nu_{ij}\theta}c^\dagger_{i\sigma}c_{j\sigma} \\ &\quad + \frac{1}{2}\sum_{i\in A}\Delta_D c^\dagger_{i\sigma}c_{i\sigma} - \frac{1}{2}\sum_{i\in B}\Delta_D c^\dagger_{i\sigma}c_{i\sigma}, \end{aligned} \quad (4)$$

where t_1 is the nearest-neighbor hopping, t_2 is the next-nearest-neighbor hopping amplitude, and U is the on site

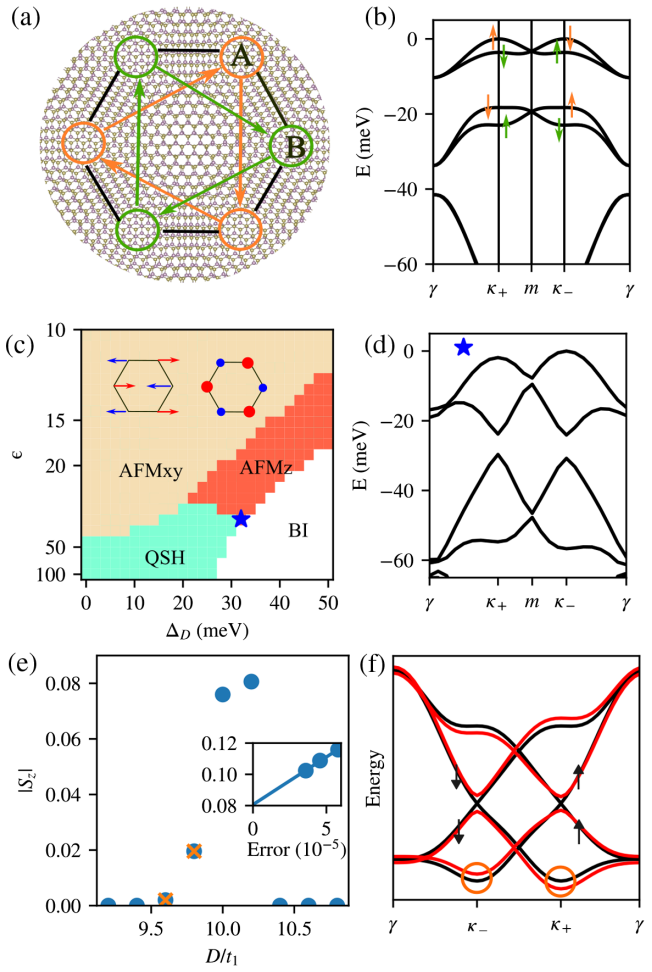

FIG. 1. (a) Real-space model for $tMoTe_2$ at 3.89°. Orange (green) circles represent MX (XM) stackings. (b) The moiré band structure with an out-of-plane electric field of $\Delta_D = 5$ meV. The orange (green) arrows indicate the states are mainly from the bottom (top) layer, and the up (down) arrows indicate spin up (down) states. (c) Phase diagram of k-space Hartree Fock calculation vs displacement field Δ_D and dielectric constant ϵ at twist angle 3.89°. In the calculations, an 18×18 mesh in the reciprocal space is used and 196 bands are included. Inset left (right) is the illustration of the in-plane (out-of-plane) spin texture of the AFMxy (AFMz) phase. (d) The quasiparticle band structure of the AFMz Chern insulator phase at $\Delta_D = 32$ meV and $\epsilon = 33$ as denoted as the blue star in (c). (e) DMRG calculation of the Kane-Mele-Hubbard model with $U = 13t_1$. The calculation is performed with bond dimensions 9600, 12 000, and 15 000. The inset shows a linear fit of order parameter over the two-site DMRG truncation errors [38] for the three bond dimensions with $\Delta_D = 10.2t_1$. Most fits yield invisible error bars except for $\Delta_D = 9.6t_1$ and $9.8t_1$ (with cross labels) with an error comparable to the values. For these two, the 15 000 bond dimension data are plotted instead. The challenges may be a consequence of nearby weak first-order transition or quantum criticality. (f) Sketch of the gap opening process of the quasiparticle band structure from the nonmagnetic phases at the QSH-BI phase boundary (black lines) to the AFMz phase (red lines). Spin orientation of the bands is denoted by black arrows.

Coulomb interaction. In Eq. (4), we have performed a particle-hole transformation, and $c^\dagger_{i\sigma}$ is the creation operator of a hole at site i with spin σ. The phase of the next-nearest-neighbor hopping is $\pm\nu_{ij}\theta$ (+ for spin up holes), where $\nu_{ij} = 1$ ($\nu_{ij} = -1$) if the hopping is along (opposite to) the direction of the arrows in Fig. 1(a). If the top four moiré bands are well separated from the remaining bands, $\theta = -\pi/3$ can be deduced from momentum mismatch via Peierls substitution [4]. The phase diagram of the Kane-Mele-Hubbard model as a function of U and Δ_D is first obtained in Ref. [43] for $\theta = \pi/2$. We obtain a similar phase diagram for $\theta = -\pi/3$; see the Supplemental Material [37]. We find the phase diagrams for the continuum model and the Kane-Mele-Hubbard model are qualitatively similar.

The Kane-Mele-Hubbard model provides a valuable starting point for understanding the phase diagram at twist angle 3.89°. At $\nu = -2$, without the electric field, each site is occupied by one electron. In the strong coupling regime, the Kane-Mele-Hubbard model can be projected into a spin model [42,44,45]:

$$H_{\text{spin}} = J_1 \sum_{\langle i,j\rangle} \boldsymbol{S}_i \cdot \boldsymbol{S}_j + \sum_{\langle\langle i,j\rangle\rangle} J_2^z S_i^z S_j^z + J_2^{xy}(S_i^x S_j^x + S_i^y S_j^y) + D(\boldsymbol{S}_i \times \boldsymbol{S}_j)\cdot\hat{\boldsymbol{z}}, \quad (5)$$

with $J_1 = 4t_1^2/U$, $J_2^z = 4t_2^2/U$, $J_2^{xy} = 4t_2^2\cos(2\theta)/U$, and $D = 4t_2^2\sin(2\theta)/U$. The direction for $\langle\langle i,j\rangle\rangle$ follows the arrows in Fig. 1(a). Therefore, J_1 is always positive, leading to antiferromagnetic interactions between the sublattices. The sign of J_2^{xy} depends on the θ. For $\theta = -\pi/3$, $J_2^{xy} < 0$, leading to the AFMxy phase in the Hartree-Fock phase diagram. For other values of θ, the translational symmetry breaking phase and spin liquid phase may appear [45].

In addition, the Kane-Mele-Hubbard model enables real-space DMRG calculations, allowing us to validate our results beyond mean field approximation for moderate size systems. We consider a three-leg armchair infinite nanotube geometry. The out-of-plane Néel order parameters $|S_z|$ of quasi-one-dimensional phases are calculated and shown in Fig. 1(e), as an indication of the intermediate AFMz phase. The AFMxy and BI can be characterized by in-plane spin-spin correlation length, which should be very large in the AFMxy region [46]. Even in the proposed AFMz region, we find that this correlation length is similar to or larger than the tube perimeter, i.e., three lattice constants. This calls for a larger-scale calculation for a quantitative inference of the 2D phase diagram.

Phase diagram at 6°.—Twisted bilayer $MoTe_2$ cannot always be characterized by a Kane-Mele-Hubbard model. For example, with increasing twist angle, a topological phase transition will happen between the second and the third topmost moiré bands. As a result, the two topmost moiré bands from the K valley will have the same Chern

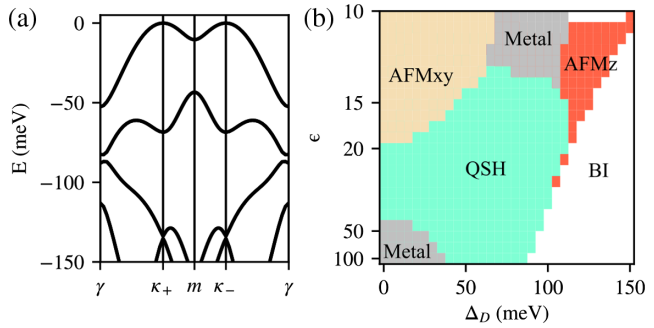

FIG. 2. (a) The noninteracting band structure at twist angle 6° without out-of-plane electric field. (b) The k-space Hartree-Fock phase diagram at twist angle 6°. In the calculations, an 18×18 mesh in the reciprocal space is used and 196 bands are included. The AFMxy and AFMz phase is still defined by the magnetic moments at MX and XM stackings, although charge density also appears at the MM stacking, where the Mo atoms sit on top of the Mo atoms.

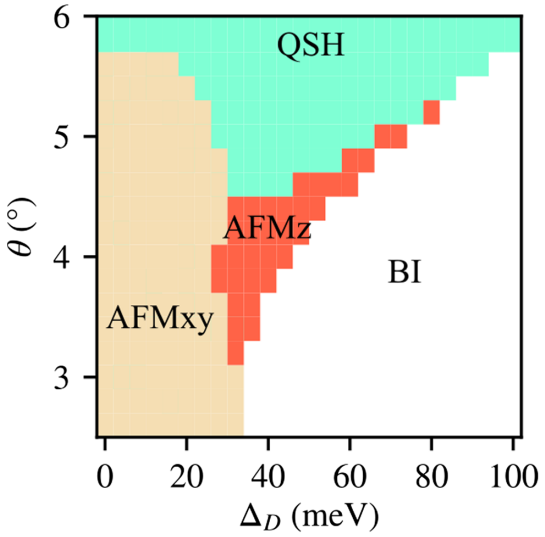

FIG. 3. The phase diagram of the continuum model at $\epsilon = 20$.

number, defying a two-orbital characterization. Even prior to the aforementioned topological phase transition, the size of the Wannier orbitals begins to diverge as the transition point is approached. Large Wannier orbitals imply the necessity of introducing intersite Coulomb interactions, including density-density interactions and exchange interactions. In all of the above senarios, the Kane-Mele-Hubbard model is insufficient for describing the electronic structure of $tMoTe_2$.

To investigate the phase diagram of $tMoTe_2$ when the Kane-Mele-Hubbard model is not useful, we carry out a Hartree-Fock calculation at twist angle 6°. The noninteracting band structure for the K valley is shown in Fig. 2(a), where the two topmost moiré bands have the same Chern number $+1$. The third topmost band is entangled with lower bands, making it even impossible to construct a three-orbital tight binding model.

In Fig. 2(b), we present the phase diagram of $tMoTe_2$ at 6°. Most phases at twist angle 3.89° can still be found at 6°. There are, however, cases where Coulomb interactions are not sufficient to open up a global gap in the Hartree-Fock calculations, and these phases are labeled as metal phases. The antiferromagnetic phase now exists at a higher external electric field, which is needed to tune the more dispersive bands at larger twist angles.

The emergence of the AFMz phase.—Figure 2(b) offers valuable clues in understanding the existence of the antiferromagnetic Chern insulator phase: the phase emerges from the boundary between the QSH phase and the BI phase. Therefore, we investigate the stability of the QSH-BI phase boundary with respect to various perturbations.

Both QSH and BI are time reversal invariant phases. As a result, the Hartree-Fock quasiparticle band energies respect $\epsilon_\alpha(\boldsymbol{k}) = \epsilon_\alpha(-\boldsymbol{k})$. Since magnetic perturbations are odd under time reversal symmetry, for a single band that is well separated from other bands by an energy gap, the first-order perturbative corrections to quasiparticle band energies satisfy $\delta\epsilon_\alpha(\boldsymbol{k}) \approx -\delta\epsilon_\alpha(-\boldsymbol{k})$ [47]. For example, the energies of the lowest band in Fig. 1(f) shift in opposite directions at $\boldsymbol{\kappa}_-$ and $\boldsymbol{\kappa}_+$ under an AFMz perturbation (black vs red lines; highlighted by orange circles). Therefore, the change of the total quasiparticle energy will be mainly contributed by the $\boldsymbol{k}$ points where the quasiparticle energies might shift above or below the Fermi energy. In particular, at the QSH-BI phase boundary, the change of the total quasiparticle energy is dominated by the gap opening at the Dirac points [see Fig. 1(f)]. Owing to the spin-split nature of the quasiparticle band structure [see Fig. 1(f)], to the first order in perturbation theory, a ferromagnetic perturbation or an antiferromagnetic perturbation in the x-y plane will not open up gaps at the Dirac points. Therefore, an antiferromagnetic perturbation in the z direction will have the best opportunity to lower the kinetic energy, leading to the AFMz Chern insulator phase.

Twist angle dependence.—The variation of twist angle changes the period of the moiré potential and serves as another tuning knob in moiré systems. In Fig. 3, we present the phase diagram where the twist angle θ is a continuous variable. It can be seen that the AFMz Chern insulator exists in a wide range of twist angles. In addition, in this phase diagram, the AFMz Chern insulator phase again originates from the QSH-BI boundary, reinforcing the heuristic argument presented above. We note that our calculations are most accurate around 3.89°, where the continuum model parameters are extracted from the density functional theory calculations.

In summary, we have discovered an antiferromagnetic Chern state in twisted bilayer $MoTe_2$ at hole doping $\nu = -2$ under an out-of-plane electric field. Experimentally, owing to a vanishing total magnetic moment, a direct or indirect measurement of Hall conductivity is required to confirm the existence of state. The easiest route is probably inferring

the Hall conductivity by the Streda formula [23], which requires the use of an external magnetic field that does not alter the system's magnetic state. For a spin model, where the local magnetic moments have fixed magnitudes, the stability of an antiferromagnetic phase under an external magnetic field is usually determined by magnetic anisotropy. In the current case, however, the magnitudes of local magnetic moments are not fixed, and the antiferromagnetic Chern state does not admit a straightforward spin model description. Further investigations are needed to determine the stability of the antiferromagnetic Chern state with respect to an external magnetic field.

We thank Xiaodong Xu for stimulating discussions. This work is mainly supported by the Center on Programmable Quantum Materials, an Energy Frontier Research Center funded by DOE BES under Award No. DE-SC0019443. The real-space Hartree-Fock calculation is supported by the Department of Energy BES QIS program under Award No. DE-SC0022277. Y. H. acknowledges support from the European Research Council (ERC) under the European Union Horizon 2020 Research and Innovation Programme (Grant Agreement No. 804213-TMCS). The DMRG calculation is performed using the TENPY [48] package. This work was facilitated through the use of advanced computational, storage, and networking infrastructure provided by the Hyak supercomputer system and funded by the University of Washington Molecular Engineering Materials Center at the University of Washington (NSF MRSEC DMR-1719797).

*These authors contributed equally to this work.
†tingcao@uw.edu
‡dixiao@uw.edu

[1] Y. Cao, V. Fatemi, S. Fang, K. Watanabe, T. Taniguchi, E. Kaxiras, and P. Jarillo-Herrero, Unconventional superconductivity in magic-angle graphene superlattices, Nature (London) **556**, 43 (2018).
[2] Y. Cao, V. Fatemi, A. Demir, S. Fang, S. L. Tomarken, J. Y. Luo, J. D. Sanchez-Yamagishi, K. Watanabe, T. Taniguchi, E. Kaxiras *et al.*, Correlated insulator behaviour at half-filling in magic-angle graphene superlattices, Nature (London) **556**, 80 (2018).
[3] F. Wu, T. Lovorn, E. Tutuc, and A. H. MacDonald, Hubbard model physics in transition metal dichalcogenide moiré bands, Phys. Rev. Lett. **121**, 026402 (2018).
[4] F. Wu, T. Lovorn, E. Tutuc, I. Martin, and A. H. MacDonald, Topological insulators in twisted transition metal dichalcogenide homobilayers, Phys. Rev. Lett. **122**, 086402 (2019).
[5] E. C. Regan, D. Wang, C. Jin, M. I. Bakti Utama, B. Gao, X. Wei, S. Zhao, W. Zhao, Z. Zhang, K. Yumigeta *et al.*, Mott and generalized Wigner crystal states in WSe_2/WS_2 moiré superlattices, Nature (London) **579**, 359 (2020).
[6] Y. Tang, L. Li, T. Li, Y. Xu, S. Liu, K. Barmak, K. Watanabe, T. Taniguchi, A. H. MacDonald, J. Shan *et al.*, Simulation of Hubbard model physics in WSe_2/WS_2 moiré superlattices, Nature (London) **579**, 353 (2020).
[7] W. Zhao, B. Shen, Z. Tao, Z. Han, K. Kang, K. Watanabe, T. Taniguchi, K. F. Mak, and J. Shan, Gate-tunable heavy fermions in a moiré kondo lattice, Nature (London) **616**, 61 (2023).
[8] T. Li, S. Jiang, L. Li, Y. Zhang, K. Kang, J. Zhu, K. Watanabe, T. Taniguchi, D. Chowdhury, L. Fu *et al.*, Continuous Mott transition in semiconductor moiré superlattices, Nature (London) **597**, 350 (2021).
[9] Y. Xu, S. Liu, D. A. Rhodes, K. Watanabe, T. Taniguchi, J. Hone, V. Elser, K. F. Mak, and J. Shan, Correlated insulating states at fractional fillings of moiré superlattices, Nature (London) **587**, 214 (2020).
[10] X. Huang, T. Wang, S. Miao, C. Wang, Z. Li, Z. Lian, T. Taniguchi, K. Watanabe, S. Okamoto, D. Xiao *et al.*, Correlated insulating states at fractional fillings of the WS_2/WSe_2 moiré lattice, Nat. Phys. **17**, 715 (2021).
[11] H. Li, S. Li, E. C. Regan, D. Wang, W. Zhao, S. Kahn, K. Yumigeta, M. Blei, T. Taniguchi, K. Watanabe *et al.*, Imaging two-dimensional generalized Wigner crystals, Nature (London) **597**, 650 (2021).
[12] T. Li, S. Jiang, B. Shen, Y. Zhang, L. Li, Z. Tao, T. Devakul, K. Watanabe, T. Taniguchi, L. Fu *et al.*, Quantum anomalous Hall effect from intertwined moiré bands, Nature (London) **600**, 641 (2021).
[13] Z. Tao, B. Shen, S. Jiang, T. Li, L. Li, L. Ma, W. Zhao, J. Hu, K. Pistunova, K. Watanabe *et al.*, Valley-coherent quantum anomalous Hall state in AB-stacked $MoTe_2/WSe_2$ bilayers, Phys. Rev. X **14**, 011004 (2024).
[14] W. Zhao, K. Kang, L. Li, C. Tschirhart, E. Redekop, K. Watanabe, T. Taniguchi, A. Young, J. Shan, and K. F. Mak, Realization of the Haldane Chern insulator in a moiré lattice, arXiv:2207.02312.
[15] Y. Zhang, T. Devakul, and L. Fu, Spin-textured chern bands in AB-stacked transition metal dichalcogenide bilayers, Proc. Natl. Acad. Sci. U.S.A. **118**, e2112673118 (2021).
[16] T. Devakul, V. Crépel, Y. Zhang, and L. Fu, Magic in twisted transition metal dichalcogenide bilayers, Nat. Commun. **12**, 6730 (2021).
[17] H. Pan, M. Xie, F. Wu, and S. Das Sarma, Topological phases in AB-stacked $MoTe_2/WSe_2$: Z_2 topological insulators, Chern insulators, and topological charge density waves, Phys. Rev. Lett. **129**, 056804 (2022).
[18] Y.-M. Xie, C.-P. Zhang, J.-X. Hu, K. F. Mak, and K. T. Law, Valley-polarized quantum anomalous Hall state in moiré $MoTe_2/WSe_2$ heterobilayers, Phys. Rev. Lett. **128**, 026402 (2022).
[19] H. Pan, F. Wu, and S. Das Sarma, Band topology, Hubbard model, Heisenberg model, and Dzyaloshinskii-Moriya interaction in twisted bilayer WSe_2, Phys. Rev. Res. **2**, 033087 (2020).
[20] M. Angeli and A. H. MacDonald, γ valley transition metal dichalcogenide moiré bands, Proc. Natl. Acad. Sci. U.S.A. **118**, e2021826118 (2021).
[21] L. Xian, M. Claassen, D. Kiese, M. M. Scherer, S. Trebst, D. M. Kennes, and A. Rubio, Realization of nearly dispersionless bands with strong orbital anisotropy from destructive interference in twisted bilayer MoS_2, Nat. Commun. **12**, 5644 (2021).

[22] E. Anderson, F.-R. Fan, J. Cai, W. Holtzmann, T. Taniguchi, K. Watanabe, D. Xiao, W. Yao, and X. Xu, Programming correlated magnetic states with gate-controlled moiré geometry, Science **381**, eadg4268 (2023).
[23] J. Cai, E. Anderson, C. Wang, X. Zhang, X. Liu, W. Holtzmann, Y. Zhang, F. Fan, T. Taniguchi, K. Watanabe *et al.*, Signatures of fractional quantum anomalous Hall states in twisted $MoTe_2$, Nature (London) **622**, 1 (2023).
[24] B. A. Foutty, C. R. Kometter, T. Devakul, A. P. Reddy, K. Watanabe, T. Taniguchi, L. Fu, and B. E. Feldman, Mapping twist-tuned multi-band topology in bilayer WSe_2, arXiv:2304.09808.
[25] H. Yu, M. Chen, and W. Yao, Giant magnetic field from moiré induced Berry phase in homobilayer semiconductors, Natl. Sci. Rev. **7**, 12 (2020).
[26] M. Haavisto, J. L. Lado, and A. Otero Fumega, Topological multiferroic order in twisted transition metal dichalcogenide bilayers, SciPost Phys. **13**, 052 (2022).
[27] Y. Zeng, Z. Xia, K. Kang, J. Zhu, P. Knüppel, C. Vaswani, K. Watanabe, T. Taniguchi, K. F. Mak, and J. Shan, Integer and fractional Chern insulators in twisted bilayer $MoTe_2$, arXiv:2305.00973.
[28] H. Park, J. Cai, E. Anderson, Y. Zhang, J. Zhu, X. Liu, C. Wang, W. Holtzmann, C. Hu, Z. Liu, T. Taniguchi, K. Watanabe, J. haw Chu, T. Cao, L. Fu, W. Yao, C.-Z. Chang, D. Cobden, D. Xiao, and X. Xu, Observation of fractionally quantized anomalous Hall effect, Nature (London) **622**, 74 (2023).
[29] F. Xu, Z. Sun, T. Jia, C. Liu, C. Xu, C. Li, Y. Gu, K. Watanabe, T. Taniguchi, B. Tong, J. Jia, Z. Shi, S. Jiang, Y. Zhang, X. Liu, and T. Li, Observation of integer and fractional quantum anomalous Hall effects in twisted bilayer $MoTe_2$, Phys. Rev. X **13**, 031037 (2023).
[30] H. Li, U. Kumar, K. Sun, and S.-Z. Lin, Spontaneous fractional Chern insulators in transition metal dichalcogenide moiré superlattices, Phys. Rev. Res. **3**, L032070 (2021).
[31] C. Wang, X.-W. Zhang, X. Liu, Y. He, X. Xu, Y. Ran, T. Cao, and D. Xiao, Fractional Chern insulator in twisted bilayer $MoTe_2$, Phys. Rev. Lett. **132**, 036501 (2024).
[32] A. P. Reddy, F. F. Alsallom, Y. Zhang, T. Devakul, and L. Fu, Fractional quantum anomalous Hall states in twisted bilayer $MoTe_2$ and WSe_2, Phys. Rev. B **108**, 085117 (2023).
[33] S. R. White, Density matrix formulation for quantum renormalization groups, Phys. Rev. Lett. **69**, 2863 (1992).
[34] I. P. McCulloch, Infinite size density matrix renormalization group, revisited, arXiv:0804.2509.
[35] D. Xiao, G.-B. Liu, W. Feng, X. Xu, and W. Yao, Coupled spin and valley physics in monolayers of MoS_2 and other group-VI dichalcogenides, Phys. Rev. Lett. **108**, 196802 (2012).
[36] S. Chatterjee, N. Bultinck, and M. P. Zaletel, Symmetry breaking and skyrmionic transport in twisted bilayer graphene, Phys. Rev. B **101**, 165141 (2020).
[37] See Supplemental Material at http://link.aps.org/supplemental/10.1103/PhysRevLett.132.146401 for additional phase diagram for the Kane-Mele-Hubbard model.
[38] S. R. White and A. L. Chernyshev, Neél order in square and triangular lattice Heisenberg models, Phys. Rev. Lett. **99**, 127004 (2007).
[39] C. L. Kane and E. J. Mele, Quantum spin Hall effect in graphene, Phys. Rev. Lett. **95**, 226801 (2005).
[40] C. L. Kane and E. J. Mele, Z2 topological order and the quantum spin Hall effect, Phys. Rev. Lett. **95**, 146802 (2005).
[41] M. Hohenadler, T. C. Lang, and F. F. Assaad, Correlation effects in quantum spin-Hall insulators: A quantum Monte Carlo study, Phys. Rev. Lett. **106**, 100403 (2011).
[42] M. Hohenadler, Z. Y. Meng, T. C. Lang, S. Wessel, A. Muramatsu, and F. F. Assaad, Quantum phase transitions in the Kane-Mele-Hubbard model, Phys. Rev. B **85**, 115132 (2012).
[43] K. Jiang, S. Zhou, X. Dai, and Z. Wang, Antiferromagnetic Chern insulators in noncentrosymmetric systems, Phys. Rev. Lett. **120**, 157205 (2018).
[44] S. Rachel and K. Le Hur, Topological insulators and Mott physics from the Hubbard interaction, Phys. Rev. B **82**, 075106 (2010).
[45] M.-H. Zare and H. Mosadeq, Spin liquid in twisted homobilayers of group-VI dichalcogenides, Phys. Rev. B **104**, 115154 (2021).
[46] D. Kiese, Y. He, C. Hickey, A. Rubio, and D. M. Kennes, TMDs as a platform for spin liquid physics: A strong coupling study of twisted bilayer WSe_2, APL Mater. **10**, 031113 (2022).
[47] The argument can be easily generalized to summations of quasiparticle band energies of nearly degenerate bands.
[48] J. Hauschild and F. Pollmann, Efficient numerical simulations with tensor networks: Tensor network Python (TENPY), SciPost Phys. Lect. Notes 5 (2018).